JGR Solid Earth

RESEARCH ARTICLE
10.1029/2024JB029010

Differential Phase Analysis for Volcanic Tremor Detection and Source Location

Andrés Barajas[1], **Nikolai M. Shapiro**[1], **and German Prieto**[2]

[1]ISTerre, Université Grenoble Alpes, CNRS, Grenoble, France, [2]Departamento de Geociencias, Universidad Nacional de Colombia, Bogotá, Colombia

Abstract We present observations showing that during episodes of volcanic tremors, the phase of inter-station cross-correlations becomes stable. We propose a new quantity, the phase coherence, to identify the differential phase stability in recordings obtained from a single pair of stations, which is extrapolated to the seismic network. Then, we present a new approach based on the estimation of differential travel times through the differential phase measurements, to locate the sources of tremors occurring at the end of 2015 at the Klyuchevskoy Volcanic Group in Kamchatka, Russia. We present evidence supporting the existence of two types of activity happening simultaneously during the tremor episode: the main tremor source, originating from a region located between 7 and 9 km depth under the main volcanoes, and the widespread occurrence of weak low-frequency earthquakes occurring at random locations. We show how the phase coherence and the differential phases can be used to provide information on the stability of the tremor source position and to estimate its location.

Plain Language Summary Volcanic tremors are a type of seismic event occurring in the vicinities of active volcanoes that are characterized by a gradual increase of energy (generally with a lack of clear impulsive signals) that can last long periods of time (from hours to months). Tremors have been associated with the pre-eruptive stages of the volcanoes, although the exact mechanism producing them remains unknown. Recent studies have also shown that the tremor activity can be used to identify the active parts of the volcanoes and to have a deeper understanding of the processes at its interior. However, the lack of clear arrivals makes it difficult to locate its sources by estimating directly the waves travel times. In this study, we propose a new approach to identify and locate the tremor sources, based on the analysis of the seismic signals in the frequency domain. We show that during a month-long tremor episode at the Klyuchevskoy Volcanic Group, the seismic activity is mainly produced by a source located close to the surface (between 7 and 9 km depth), and by earthquakes occurring at a wide range of depths.

Key Points:

- Differential phase between station pairs becomes stable during tremor episodes
- Travel times measured from the differential phase are used to locate tremor sources
- Tremor sources illuminate an active trans-crustal magmatic system

Supporting Information:

Supporting Information may be found in the online version of this article.

Correspondence to:

A. Barajas,
andres.barajas-ramirez@univ-grenoble-alpes.fr

Citation:

Barajas, A., Shapiro, N. M., & Prieto, G. (2024). Differential phase analysis for volcanic tremor detection and source location. *Journal of Geophysical Research: Solid Earth*, *129*, e2024JB029010. https://doi.org/10.1029/2024JB029010

Received 26 FEB 2024
Accepted 14 OCT 2024

Author Contributions:

Conceptualization: Andrés Barajas, Nikolai M. Shapiro, German Prieto
Data curation: Andrés Barajas
Formal analysis: Andrés Barajas, Nikolai M. Shapiro
Funding acquisition: Nikolai M. Shapiro
Investigation: Andrés Barajas
Methodology: Andrés Barajas, Nikolai M. Shapiro, German Prieto
Project administration: Nikolai M. Shapiro
Resources: Andrés Barajas
Software: Andrés Barajas
Supervision: Nikolai M. Shapiro
Validation: Andrés Barajas
Visualization: Andrés Barajas
Writing – original draft: Andrés Barajas

1. Introduction

Seismic activity in volcanic environments consists of a wide range of different phenomena related to complex geological and chemical processes. One of them, volcanic tremors, is usually recorded as emerging signals without a clear onset, contrary to the regular earthquakes (e.g., Konstantinou & Schlindwein, 2002; McNutt & Nishimura, 2008; N. M. Shapiro et al., 2024). They have been observed to last for periods that range from hours to months, between 1 and 8 Hz, which is usually lower than the characteristic frequencies of small volcano-tectonic earthquakes (e.g., Roman & Cashman, 2006). Volcanic tremors are often considered to be formed by high-rate emissions of low-frequency volcanic earthquakes (e.g., Fehler, 1983). Low-frequency volcanic seismicity is generally related to the magmatic or hydrothermal fluid pressure variations within the volcano plumbing systems (e.g., Chouet, 1996), although its exact mechanism is still investigated. Overall, tremors are an important indicator of volcanic unrest, and a tool to help to monitor and forecast eruptions (e.g., Caudron, Aoki, et al., 2022) and to image the inner structure of the magmatic system (e.g., Journeau et al., 2022).

Because of the lack of identifiable arrivals, the tremors cannot be analyzed with the same methods as regular earthquakes. Most often, they are detected based on the increased amplitude of the signal at a given station (e.g., Endo & Murray, 1991). Alternatively, network-based methods of analysis based on inter-station cross-correlations have shown to be effective in identifying tremor occurrences and locating their sources (e.g., Almendros et al., 1997; Ballmer et al., 2013; Barajas et al., 2023; Droznin et al., 2015; Journeau et al., 2020, 2023; Kuperman & Turek, 1997; Nanni et al., 2021; Seydoux et al., 2016; Soubestre et al., 2018, 2019, 2021). The

Writing – review & editing:
Andrés Barajas, Nikolai M. Shapiro, German Prieto

mentioned studies explore either the amplitudes of the inter-station cross-correlation functions or properties of the network covariance matrix. In this study, we propose a new approach that directly analyzes the phase of the cross-correlation function computed between a pair of stations that we will refer in this paper as "differential phase." First, we show that the differential phase stabilizes during tremor episodes. After, we propose a way to quantify the stability of the differential phase that we call "phase coherence," which can be efficiently used to detect tremors. Then, we use the differential phases to estimate differential travel times between pairs of stations. These measurements combined for a network of stations are then used to locate tremor sources.

We apply the proposed method to continuous records of seismic stations installed during 2015–2016 in the framework of the KISS experiment (Klyuchevskoy Investigation—Seismic Structure of an Extraordinary Volcanic System, N. M. Shapiro, Sens-Schönfelder, et al., 2017) in Kamchatka, Russia. In particular, we focus on a strong tremor observed in December 2015–January 2016. We show that the differential phase method allows both the identification of tremor episodes and the location of their sources. Based on physical considerations of the differential phase stability, direct observations, and the tremor source locations, we identify two distinct groups of tremor sources. The first group remains relatively stable at shallow depths (above 9 km). The second group consists of more episodic and widespread activity occurring through a large range of depths.

2. Klyuchevskoy Volcanic Group and Its Seismicity

The Klyuchevskoy Volcanic Group (KVG) is one of the largest and most active volcano clusters in the world (e.g., N. M. Shapiro, Sens-Schönfelder, et al., 2017). It is located in the Kamchatka peninsula, Russia, under the subducting Pacific plate. Elevated volcanic activity in this region is related to the unique tectonic setting at the corner between the Kuril-Kamchatka and Aleutian trenches (e.g., Levin et al., 2002; Portnyagin et al., 2005). The enhanced supply of magmas from the mantle can be caused by the around-slab-edge asthenospheric flow (Levin et al., 2002; Yogodzinski et al., 2001) and related crustal extension (Green et al., 2020; Koulakov et al., 2020) or by fluids released from the thick, highly hydrated Hawaiian-Emperor crust subducted beneath this corner (Dorendorf et al., 2000).

The diversity of seismic activity in the area is often attributed to magma transfer processes (e.g., Dobretsov et al., 2012; S. Fedotov & Zharinov, 2007; S. A. Fedotov et al., 2010; Senyukov et al., 2009) and pressure transients (e.g., Frank et al., 2018; N. M. Shapiro, Droznin, et al., 2017) occurring through a large-scale magmatic system connecting different volcanoes of the KVG (Coppola et al., 2021). Long-period earthquakes beneath the KVG have been located at shallow depths (~5 km) and at deeper zones (~30 km) (e.g., Galina & Shapiro, 2024; Galina et al., 2020; Levin et al., 2014; N. M. Shapiro, Droznin, et al., 2017). The deeper zone has been associated with a strong Vp/Vs anomaly (e.g., Ivanov et al., 2016; Koulakov et al., 2017), most probably produced by a magma reservoir inserted in the crust-mantle transition (e.g., Green et al., 2020; Koulakov et al., 2020).

The KVG volcanic activity is accompanied by strong and long-duration seismic tremors both during the eruptions and their preparation periods. The locations of the sources of different tremor episodes at the KVG have been done through the envelopes of the cross-correlations (e.g., Droznin et al., 2015) showing that the active part of the magmatic system under the volcanic group extends over a wide range of crustal depths, that experience seismic activations probably as a result of rapid pressure migrations between them (e.g., Journeau et al., 2022; Soubestre et al., 2019).

3. The Data

We use continuous vertical component velocity seismograms recorded at the seismic stations shown in Figure 1, between May 2015 and October 2016. This network consists of stations from the permanent network managed by the Kamchatka Branch of Geophysical Survey (KBGS) and from the temporary network station installed under the project Klyuchevskoy Investigation—Seismic Structure of an Extraordinary Volcanic System (KISS) (N. M. Shapiro, Sens-Schönfelder, et al., 2017).

3.1. Data Preprocessing

The continuous seismograms are stored in daily records. For each record, the mean and the linear trend are removed. Afterward, they are band-passed between 0.01 and 10 Hz and downsampled to 25 samples per second.

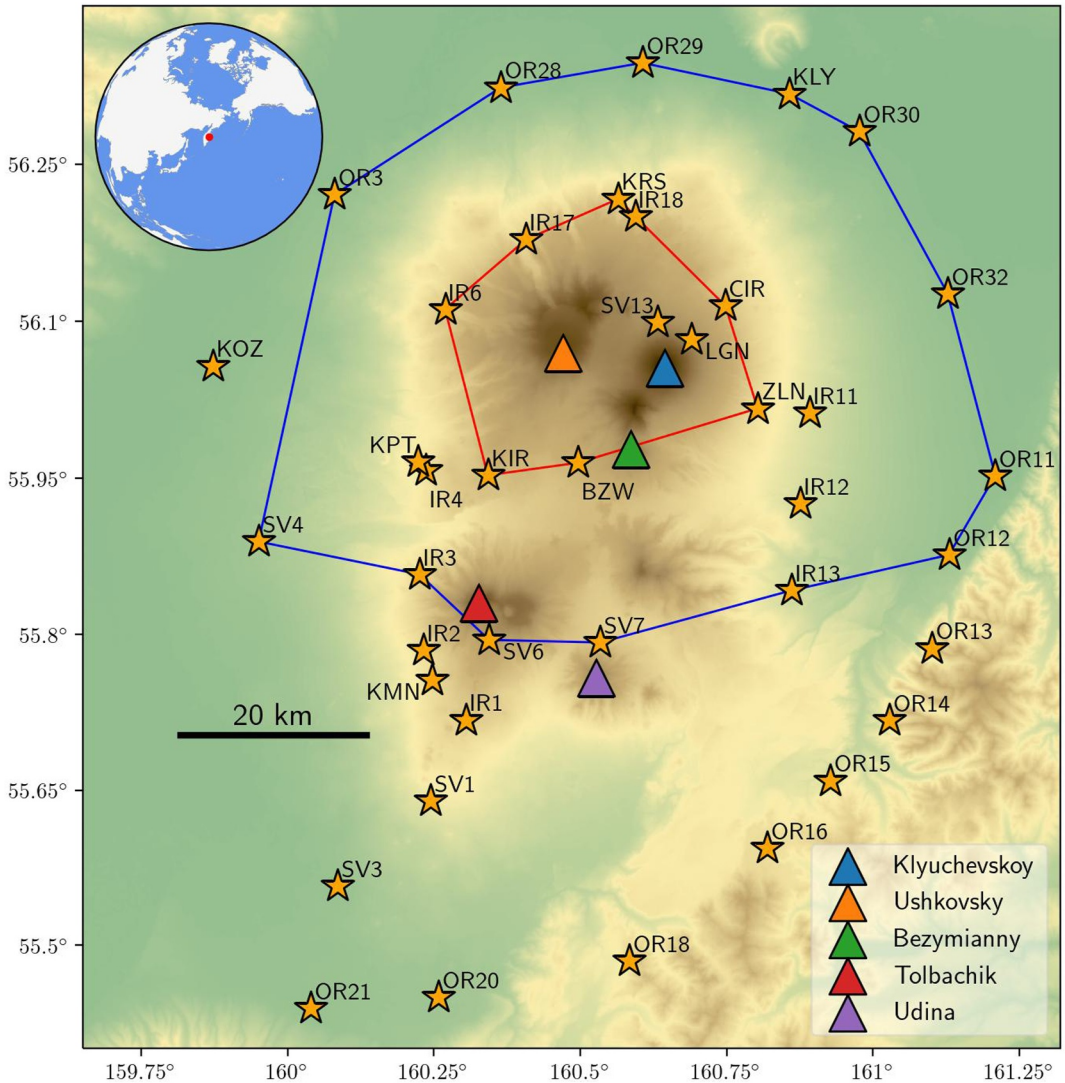

Figure 1. Klyuchevskoy Volcanic Group in the peninsula of Kamchatka, Russia. The triangles represent the active volcanoes. The stars represent the stations from the permanent and temporary seismic networks. The red and blue lines link the pairs of adjacent stations used for the calculation of the coherence in Figure 7.

The records for each station i, are then divided into windows of duration $\widetilde{\delta t} = 40$ s, with an overlap of 50% (20 s), tapered with a Hanning window and transformed into the frequency domain.

4. Methods

4.1. Cross-Correlations and Cross Spectra

The seismic network consists of N stations and produces N continuous recordings which can be divided into windows of duration $\widetilde{\delta t}$. We refer to each of these windows recorded at station i as $u_i(t)$. The frequency representation of these time series, obtained through the Fourier Transform:

$$\mathbf{U}_i(f) = \widetilde{\mathcal{F}}(u_i(t)) \tag{1}$$

which can be described in terms of its magnitude r_i and phase φ_i as:

$$\mathbf{U}_i(f) = r_i(f)e^{i\varphi_i(f)} \tag{2}$$

The phase $\varphi_i(f)$ depends on the source mechanism and on the propagation of seismic waves between the source and the station. The amplitude factor $r_i(f)$ is a combination of the source intensity with the interference pattern between multiply scattered arrivals. This interference pattern strongly amplifies some spectral peaks (Barajas et al., 2023). The multiplication between the Fourier Transform of the signal at one station $\mathbf{U}_i(f)$, and the complex conjugate at another station $\mathbf{U}_j^{\dagger}(f)$ gives a complex cross-spectrum (the Fourier domain representation of the cross-correlation function):

$$\mathbf{C}_{i-j}(f) = \mathbf{U}_i(f)\mathbf{U}_j^{\dagger}(f) = r_i(f)r_j(f)e^{i\Delta\varphi_{i-j}(f)} \tag{3}$$

where $\Delta\varphi_{i-j}(f)$ is the differential phase between these two stations. This differential phase remains stable if the source position and mechanism do not change. The amplitude factor $r_i(f)r_j(f)$ is dominated by the combination of two interference patterns of multiply scattered waves, resulting in multiple spectral peaks. The position of these peaks remains stable for unchanged source position and mechanism (Barajas et al., 2023). The cross-spectrum, $\mathbf{C}_{i-j}(f)$, is the Fourier Transform of the cross-correlation between station i and j, $\mathbf{C}_{i-j}(\tau)$, as is shown in the convolution theorem (McGillem & Cooper, 1991):

$$\mathbf{C}_{i-j}(f) = \mathfrak{F}(u_i(t) \star u_j(t)) = \mathfrak{F}(\mathbf{C}_{i-j}(\tau)) \tag{4}$$

where $\star$ represents the cross-correlation operation, and τ is the lag time of the cross-correlation. Given that the cross-spectrum is calculated for several overlapping windows centered at different times, we use the notation $\mathbf{C}_{i-j}(f,t)$ to refer to the cross-spectrum calculated between stations i and j with the windows that begin at time t, and $\mathbf{C}_{i-j}(\tau,t)$ to refer to the cross-correlation calculated with the same windows.

We will mostly focus on the differential phase $\Delta\varphi_{i-j}(f,t)$. Our first observation is that it behaves very differently for records containing noise and tremors. In the first case, the differential phase is randomly distributed, while it is relatively stable in the second. The stability of the differential phase is a consequence of a fixed tremor source position and constant travel times. Later, the inter-station differential phases are used to compute inter-station travel times and to locate the tremor sources.

4.2. Differential Phase Stability

Figure 2 shows seismograms recorded at two stations during 4 days corresponding to the beginning of a tremor episode occurring between December 2015 and January 2016 (Journeau et al., 2022). The continuous seismic records for stations IR18 and SV13 (Figures 2a and 2c respectively) show the characteristic non-impulsive slow onset of seismic energy of tremor episodes. The recordings are divided into small windows and the Fourier Transform is applied over each of them, as described in Section 3.1; Figures 2b and 2d show the phases of individual seismograms at a frequency of 0.5 Hz. For both stations, these phases remain random during the whole considered period. However, it can be seen in Figure 2e that the differential phase between two stations (Equation 3) develops a clear non-random behavior nearly simultaneously with the emergence of the tremor. The concentration of the differential phase around a certain level during long periods will be referred to as the differential phase time stability, or simply phase stability, between the two stations. As explained in the previous section, the stability of the phase implies that the tremor source mechanism remains stable and that its position is constrained to certain points in the medium during this period. To identify this phenomenon at different frequencies, and to estimate the mean value around which the differential phase stabilizes, we propose two possible measurements based on the circular extrinsic mean (Hotz, 2013).

The cross-spectrum at a given frequency and time can be represented as a vector in the complex plane with its angle relative to the horizontal (real) axis being the differential phase, as shown in Figure 3. If the registered wavefield is dominated by noise (as in the case depicted in Figure 3a) the differential phases will be random, which implies that the vectors representing the cross-spectra point in random directions. Therefore, the sum of many cross-spectra over the complex plane will have a small magnitude compared with the sum of the individual magnitudes (red arrow in Figure 3a). On the other hand, if a tremor event dominates the registered wavefield, the differential phase is approximately constant, which implies that the vectors representing the cross-spectra point

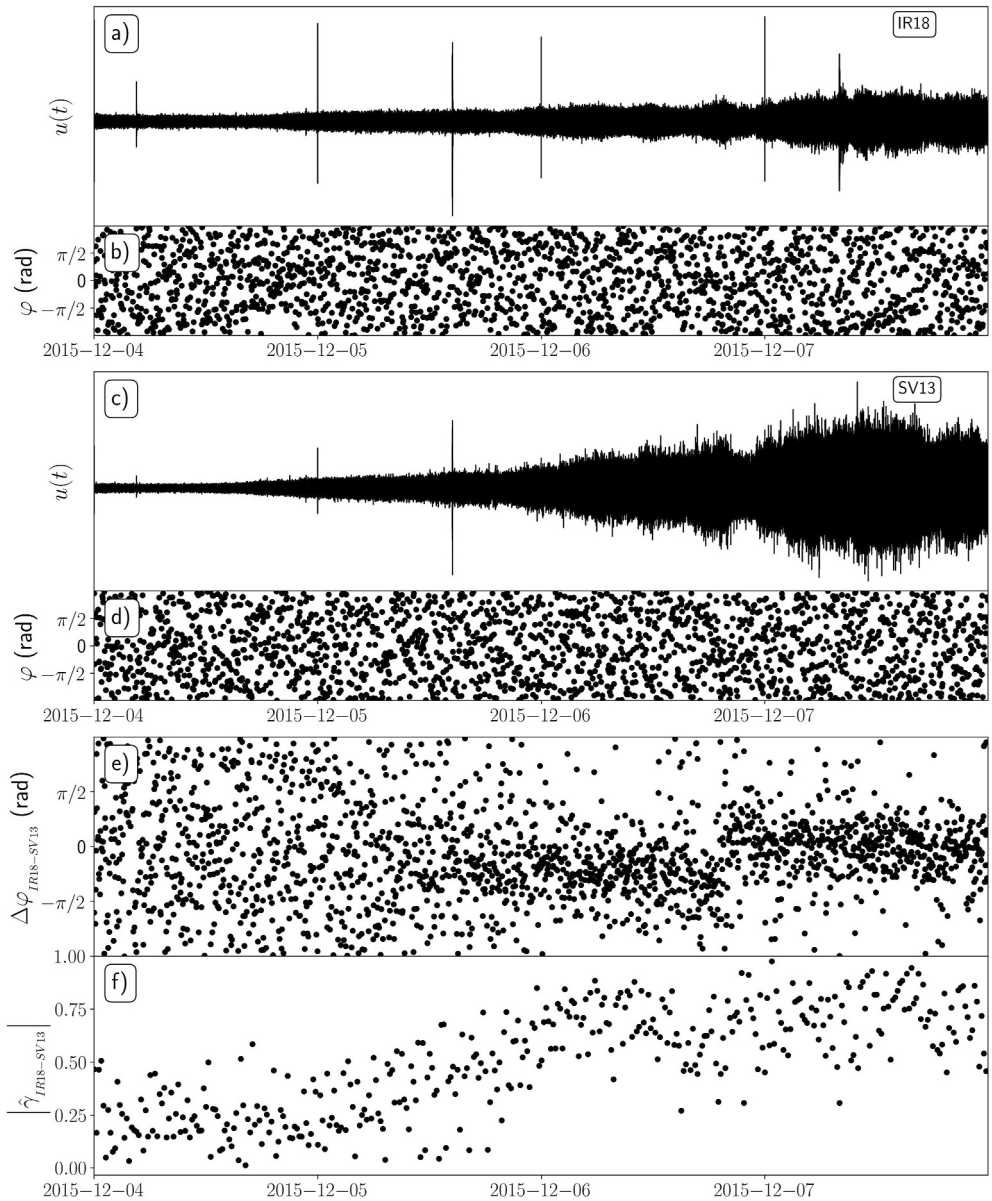

Figure 2. Phase stability observations. Continuous seismic recordings band-passed between 0.3 and 5 Hz, during 4 days at the beginning of a tremor episode at stations IR18 (a) and SV13 (c). The phases of overlapping 40-s windows at 0.5 Hz during this period for station IR18 (b) SV13 (d) are random. However, the differential phase $\Delta\varphi$ between stations IR18 and SV13 at 0.5 Hz (e) shows a non-random behavior after the beginning of the tremor episode. The simplified coherence, $|\hat{\gamma}|$, between stations IR18 and SV13 at 0.5 Hz (f) quantifies the stability of the phase.

approximately in the same direction (as in the case depicted in Figure 3b). In this case, the sum of the cross-spectra will have a magnitude comparable with the sum of the individual magnitudes (blue arrow in Figure 3b).

These two simple scenarios suggest that the sum or the mean of the cross-spectra over many windows, can be used as a discriminator to identify the stability of the differential phase. However, there are two problems with this approach: first, a signal can have very different levels of energy at different frequencies, which means that it is possible to have a stable differential phase at two frequencies, and at the same time obtain very different magnitudes of the cross-spectra average. Second, suppose that an earthquake occurs during a period with no tremors. In that case, the resulting magnitude of the cross-spectra sum will be large despite the fact that the phase is not stable, making it indistinguishable from the case with tremors. To address these problems, we propose two normalization methods.

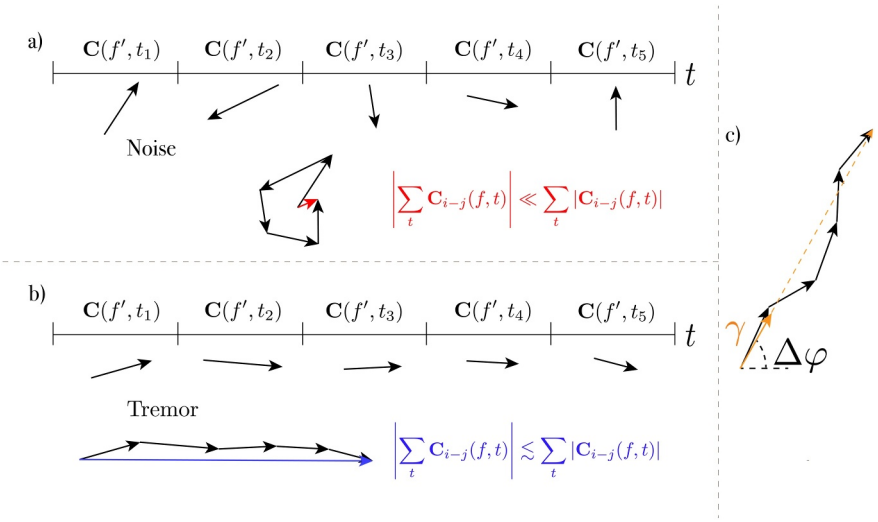

Figure 3. Schematic representation of the cross-spectra for the case where the wavefield is dominated by (a) noise, (b) tremor events. (c) Relation between the phase coherence γ and the differential phase $\Delta\varphi$.

4.2.1. Simplified Phase Coherence

The first consists of normalizing the cross-spectrum of each window before adding them together:

$$\hat{\mathbf{C}}_{i-j}(f,t) = \mathbf{C}_{i-j}(f,t)/|\mathbf{C}_{i-j}(f,t)| \Rightarrow \left|\hat{\mathbf{C}}_{i-j}(f,t)\right| = 1 \tag{5}$$

We define the simplified phase coherence (or simplified coherence, for simplicity) as the average of these normalized cross-spectra:

$$\hat{\gamma}_{i-j}(f,t_0) = \frac{1}{N}\sum_{n=0}^{N} \hat{\mathbf{C}}_{i-j}(f,t_n) \tag{6}$$

where N represents the number of windows included in the sum. The simplified coherence between stations i and j, is a complex-valued function of frequency and time. The argument t_0 is the time at which the first window of the summation begins. In analogy to the notation used for the cross-correlations, the phase coherence in the time domain will be represented by $\hat{\gamma}_{i-j}(\tau,t_0)$, where τ is the lag time. This is a reformulation of the very well-known random walk problem in two dimensions (Hughes, 1996, p. 53) whose probability for many steps follows a Rayleigh distribution (Wolfgang & Baschnagel, 2013, p. 69). The random walk problem has been adapted to analyze the tidal triggering of earthquakes (Heaton, 1975; Schuster, 1897), the distribution of events on a catalog (Rydelek & Hass, 1994) or to identify colocated earthquakes and tremors (Hawthorne & Ampuero, 2018), where the quantity is known as phase walkout.

In the present study, we calculate the simplified coherence over a large window composed of $n_w = 45$ windows of $\widetilde{\delta t} = 40$ seconds, with an overlap o of 50%. Each of these large windows used to calculate the coherence, which we will refer to as the averaging window, has a duration of $\widetilde{\delta T} = n_w\left(\widetilde{\delta t}\right)o = 15$ min.

As a consequence of the applied normalization, the amplitude of the simplified coherence is always between 0 and 1. When at a certain frequency f', the registered seismic field is dominated by noise, then $\left|\hat{\gamma}_{i-j}\left(f',t\right)\right| \approx 0$. On the contrary, when the phase is highly stable, then $\left|\hat{\gamma}_{i-j}\left(f',t\right)\right| \approx 1$. The simplified coherence depends only on the phase of the signals and not on their amplitude. Figure 2f shows that the simplified coherence for the station pair IR18-SV13 at 0.5 Hz, successfully quantifies the stabilization of the differential phase.

Figure 4a shows the simplified coherence amplitude for the station pair IR18-SV13 between 0.3 and 5 Hz. While the phase stability occurs in a broad range of frequencies, its behavior is very irregular with many narrow spectral

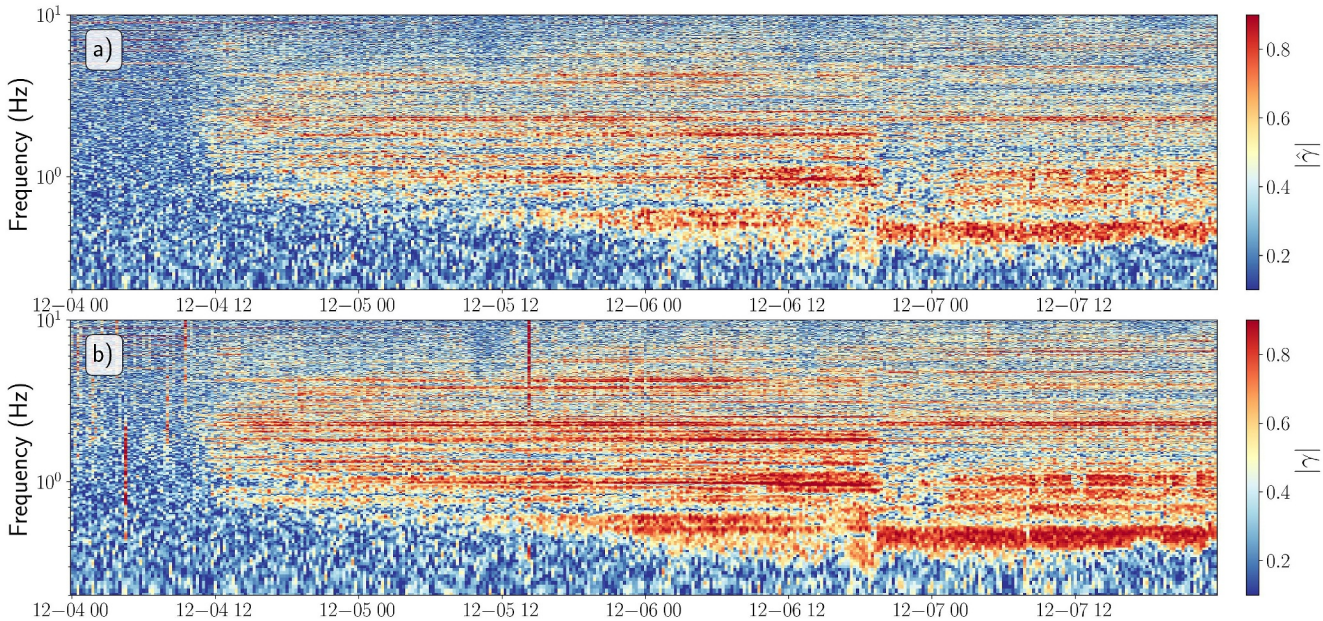

Figure 4. (a) Simplified phase coherence and (b) phase coherence, for station IR18-SV13, during the same period of Figure 2.

bands, similar to the coherent spectral lines observed during volcanic tremors with the covariance matrix method (e.g., Barajas et al., 2023; Caudron, Soubestre, et al., 2022; Journeau et al., 2020, 2022; Soubestre et al., 2018, 2021). Many of these lines remain fixed for several hours, likely indicating that some of the tremor-generating processes remain "stable" over long periods. At the same time, the change in the spectral content of tremor is systematically observed, likely indicating modifications of the state of some parts of the active plumbing system. Sometimes these changes are progressive, like the emergence of new lines at low frequencies at around noon on December 5. In other cases, it can be very rapid, like the abrupt change of the lines structure at almost all frequencies as it occurs around 20hr on December 6.

Earthquakes or high energetic seismic signals with durations shorter than 40 s, do not affect the simplified coherence because their amplitude is removed, meaning that they are not detectable under this normalization. However, the simplified phase coherence does not take advantage of the tremor energy levels being higher than the noise energy levels, as it removes any amplitude information. To exploit this characteristic feature of tremors, we propose a second normalization.

4.2.2. Phase Coherence

The second normalization method consists in dividing the cross-spectrum by the auto-spectra of each signal (that are real-valued). We call the resulting complex function phase coherence:

$$\gamma_{i-j}(f,t_0) = \frac{\frac{1}{N}\sum_{n=0}^{N} \mathbf{C}_{i-j}(f,t_n)}{\sqrt{\left(\frac{1}{N}\sum_{n=0}^{N} \mathbf{C}_{i-i}(f,t_n)\right)\left(\frac{1}{N}\sum_{n=0}^{N} \mathbf{C}_{j-j}(f,t_n)\right)}} \tag{7}$$

The argument t_0 is the time at which the first window of the summation begins. It is important to note that although this definition is similar to the classical coherence (Prieto, 2022), in this case, the sum is not defined over a single window (multiplied with different tapers) but over several windows, to evaluate the phase similarity between them. The classical coherence is not calculated in this study and therefore, we will use the term coherence to refer to phase coherence for simplicity.

It is clear from Equation 7 that the phase coherence can be interpreted as a normalized average cross-spectrum. As shown in Figure 4b, the coherence magnitude produces higher values than the simplified coherence, as it includes

both the phase and the amplitude of the tremor signals. However, this also has the effect of highlighting the earthquakes, as can be seen around 2015-12-04h04 or 2015-12-04h13 where there are now single averaging windows with high coherence. Earthquakes may also decrease the overall coherence when they occur simultaneously with tremors because their complex spectra may have different orientations, canceling each other at certain frequencies. Automatic classification between noise, earthquakes, and tremors can be easily done by comparing the simplified coherence and the coherence for the same period: the first case (noise) will not produce high coherence in any case, the second (earthquake) will produce high values of coherence but not of simplified coherence, and the third case (tremor) will produce high values for both coherence.

There are some similarities in terms between the method developed in this study and the Matched Field Processing (MFP) (Baggeroer et al., 1993; Hawthorne & Ampuero, 2018; Schippkus & Hadziioannou, 2022; Wang et al., 2015). At the same time, the two approaches are different. For this reason, we provide a comparison between the two methods in Appendix A. Additionally to inter-station coherences, inter-component coherences from single stations could be used to detect tremors (e.g., Gombert & Hawthorne, 2023; Journeau et al., 2020; Yates, 2023).

4.3. Differential Travel Times

An important property arises if we assume that one of the signals is a time-shifted version of the other, $u_j(t) = u_i(t - \Delta t_{i-j})$, with Δt_{i-j} representing the delay or differential travel time between the two signals. By applying the time-shift property of the Fourier Transform (Margrave & Lamoureux, 2019, p. 76), the cross-spectrum can be written as

$$\mathbf{C}_{i-j}(f) = r_i^2(f)e^{-i2\pi\Delta t_{i-j}f} \tag{8}$$

By matching Equations 3 and 8 we obtain that

$$\Delta\varphi_{i-j}(f) = -2\pi\Delta t_{i-j}f \tag{9}$$

The determination of the differential travel times as the slope of the relation between the differential phase and the frequency has been extensively used to locate repeating events (e.g., Frechet, 1985; Ito, 1985; Poupinet et al., 1984), microearthquake clusters (e.g., Deichmann & Garcia-Fernandez, 1992; Got et al., 1994), foreshocks and aftershock sequences (e.g., Dodge et al., 1995; Shearer, 1997), as well as to hypocenter location optimization (e.g., Schaff et al., 2004) and correction with the double-difference method (e.g., Waldhauser & Ellsworth, 2000). This approach also has been extensively used in the noise-based seismic interferometry (e.g., Brenguier, Campillo, et al., 2008; Brenguier, Shapiro, et al., 2008; Clarke et al., 2011). Travel time differences Δt_{i-j} can be also estimated from the time representation of the cross-correlations (Michele et al., 2020; Valoroso et al., 2013), which can be more robust and reliable for clearly impulsive signals (Schaff et al., 2004). However, this is not the case with emergent signals like tremors where independent arrivals are not easily distinguishable.

The phase coherences, γ and $\hat{\gamma}$, play a double role in our analysis. On one hand, the magnitude of the phase coherences is related to the differential phase stability and therefore to the coherence of the wavefield as was shown in Section 4.2. On the other hand, the argument (or angle) of the phase coherence is the mean differential phase of the cross-spectra within the averaging window, as illustrated in Figure 3c

$$\Delta\varphi_{i-j} = \arg(\gamma_{i-j}) \tag{10}$$

Therefore, the estimation of the differential travel times for each date starts by computing the phase coherence γ for each station pair as described in Section 4.2.2. Then, the differential phases are estimated with Equation 10. The coherence is used from this point forward, as it highlights the presence of tremors better than the simplified coherence.

A first filter is applied by removing the differential phase points that are not stable enough ($|\gamma| < 0.35$), as shown in Figure 5a. This value was found by inspection, and it is case-dependent as it quantifies the degree of phase variability on the recorded signals, which depends on the noise levels. This procedure creates "holes" or discontinuities in the frequency range (in this case 0.35–5 Hz), leaving smaller sets of contiguous frequencies at

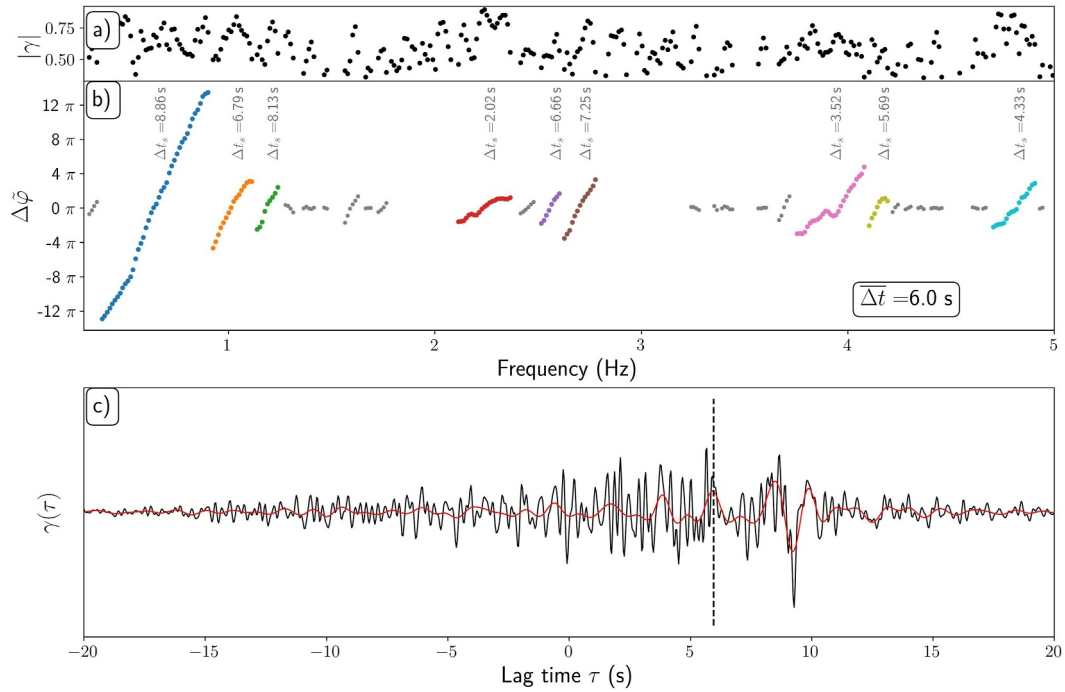

Figure 5. Phase coherence and differential phase between stations IR18 and SV13 for the 2015-12-07h06:15. (a) Amplitude of the phase coherence $|\gamma|$. (b) Differential phase sets and their respective differential travel times. (c) Phase coherence in the temporal domain band-passed between 0.3 and 5 Hz (black line) and between 0.3 and 1 Hz (red line). The average differential travel time obtained by measuring the slopes is signaled with the dashed line.

which the differential phase is stable (Figure 5b). In the next step, the frequency intervals with less than 8 contiguous points, shown as the gray dots in Figure 5b, are discarded. For each of the remaining intervals, a linear regression is performed between the differential phases and the frequencies to calculate the differential travel times (Equation 9). Then, the intervals where the correlation coefficient ρ is lower than 0.9 are discarded, as this indicates low linearity between the variables, possibly produced by the presence of multiple sources or unreliable relative phase values.

The remaining intervals of this filtering process are represented by different colors in Figure 5b with their respective differential travel times (Δt_s) marked over each of them. Finally, an estimation of differential travel time between the two stations is obtained as a weighted average:

$$\overline{\Delta t} = \frac{\sum_s n_s \Delta t_s}{\sum_s n_s} \tag{11}$$

where Δt_s is the differential travel time and n_s is the number of points of every set (s) of contiguous frequencies. The numbers of points are used as weights because larger continuous sets provide more reliable slope estimations. A positive differential travel time, as shown in this case, indicates that the second station of the pair (CIR) is closer to the source. This depends on the order of the stations because the cross-correlation (Equation 4) is not a commutative operation. Inverting the order of the stations of the cross-correlations will invert the directions of the slopes in Figure 5b, without affecting the physical interpretation of the relative position of the stations to the source.

There are practical and physical reasons to treat the continuous sets independently, instead of unwrapping all the phase points together and estimating a unique differential travel time from them. The first reason is practical: when the gap between contiguous sets is too big in the frequency domain, the expected phase correction may be larger than 2π, rendering the unwrapping operation incapable of introducing a reliable shift between the sets. This is the case of Figure 5b between 1.2 and 2.1 Hz. The other reason comes from physical considerations: different sources may produce different contiguous intervals of stable phase. In this case, the differences in the differential

travel times would be a natural consequence of these sources having different positions within the volcanic system. If the travel times measured in these intervals are similar, then the positions of their sources are close to each other. Another possibility is that the tremor is generated by a single source located in a heterogeneous medium. The emitted radiation would scatter, creating packages of coherent waves that reach the receiver with possibly slightly different travel times and interfere with each other. This interference would result in a complex Fourier spectrum and explain why the differential phase is stable only in certain frequency gaps. Sharp slope variations are also to be expected if at different frequencies the wavefield is dominated by different types of waves (e.g., surface, body waves). Note that in any case, even when the frequency gaps are small, treating all the intervals together (instead of analyzing them separately) may result in a strong bias because the linear regression is made under the assumption of a common slope for the data, which may not be the case as is illustrated in Figure 5b. For simplicity, we assume that the signal is produced by a single source (or by closely located sources) by averaging the differential travel times. This justifies the application of Equation 11.

Figure 5c shows the phase coherence γ in the time domain (which can be interpreted as an average cross-correlation) between stations IR18 and SV13, band-passed between 0.35 and 5 Hz, represented by a black line. The average differential travel time obtained by measuring the slopes $\overline{\Delta t} = 6\ s$ and applying Equation 11 is indicated with the dashed line. Occasionally, individual arrivals can be easily identified in both the frequency and the temporal domain: this is the case of the set of blue set of points in Figure 5b which corresponds to the high amplitude arrival at 9 s in Figure 5c. This arrival is highlighted in the time domain when the phase coherence is band-passed between 0.35 and 1 Hz, represented by the red line in Figure 5c. However, it is important to note that the estimation of the differential travel time is obtained with a subset of the points in the frequency range, while the signal shown in Figure 5c is calculated using all the frequencies after the band-pass, and therefore, differences between the two are to be expected.

Comparison of Figures 5b and 5c show that the differential travel time estimation obtained from the phase coherence is relatively close to the one that could be estimated from the cross-correlation maximum and used in some previous studies. This implies that the estimation based on Equation 11 is a good alternative to the amplitude-based estimation. At the same time, it is important to remember that both amplitude and phase-based estimations depend on several parameters selected for the data pre-processing and for computing the cross-correlations and the phase coherences in the time and frequency domains. Overall, these estimations of differential times for tremors are associated with important uncertainties and are less accurate than travel times that can be measured for impulsive arrivals recorded for regular earthquakes.

4.4. Source Location

The source is located through a back-projection grid search. For the KVG/KISS data set the grid extends over 300 km in the west-east direction, 200 km in the north-south direction, with the vertical axis ranging from 5 km altitude to 50 km depths, with a spacing of approximately 2.5 km on each direction. We compute travel times from every position in the grid to every station in the network using the TauP Toolkit package (Crotwell et al., 1999) with the 1-D model velocity of Journeau et al. (2022), assuming that tremors are dominated by *S*-wave energy. Then, the differential times Δt_{i-j} are calculated from each position in the grid. At this point, another filter is applied: the location of the source is estimated only for the dates where the number of station pairs that remain after the previous filtering processes $\tilde{N}_p$ (described in the previous section) is greater than 100. This is done to avoid unreliable source locations obtained through small sets of station pairs. For each position of the grid, the error is calculated as the average of the absolute differences between the differential travel times obtained through the 1D model ($\Delta t_{i-j,1\mathrm{D}}$), and the measurement of the differential phases slopes in the frequency domain ($\Delta t_{i-j,\Delta\varphi}$)

$$E_r(\mathbf{r}) = \frac{1}{\tilde{N}_p} \sum_{\tilde{N}_p} |\Delta t_{i-j,1\mathrm{D}}(\mathbf{r}) - \Delta t_{i-j,\Delta\varphi}| \tag{12}$$

where and $\mathbf{r}$ represents the position of each point in the grid. The mean absolute error (L1 norm) is used to avoid over-representing the outliers, which are common through this procedure. The position of the source is chosen as the point with the lowest error. Finally, the sources located at the lower and lateral border of the grid are removed. All the processing steps are summarized in Table 1.

Table 1
Source Location Procedure With the Differential Phase, With a General Description of Each Step and the Parameter Values Used on This Study

	Description	Parameters
1.	For each station i, divide the continuous seismic record in small windows $u_i(t)$ of duration $\widetilde{\delta t}$ and apply to each of them the Fourier transform to obtain $\mathbf{U}_i(f)$	$\widetilde{\delta t} = 40$ s
2.	Calculate all the possible cross-spectrum in the frequency domain $\mathbf{C}_{i-j}(f)$ (Equation 3)	–
3.	The phase coherence γ (Equation 7) is calculated over an averaging window of duration $\widetilde{\delta T}$ using n_w small windows with an overlap r	$\widetilde{\delta T} = 15$ min, $n_w = 45$, $r = 0.5$
4.	For each pair of stations, the differential phase is obtained as the angles of the phase coherence within a frequency range	$0.35 < f < 5$ Hz
5.	The differential phase points $\Delta\phi$ are filtered with a condition over $\lvert\gamma\rvert$ (Figure 5a)	$\lvert\gamma\rvert > 0.35$, $0.3 > \lvert\gamma\rvert > 0.9$
6.	The remaining differential phase points are grouped into sets of contiguous points. The sets with less than 8 points are removed (gray dots in Figure 5b)	$n_s > 8$
7.	The sets with correlation coefficients lower than 0.9 are discarded	$\rho > 0.9$
8.	The differential times for each set, Δt_s, are calculated as the slope between the differential phases and the frequencies (Equation 9, Figure 5b)	–
9.	The total differential time for each pair of stations is calculated as the weighted average of the differential times of all sets (Equation 11)	–
10.	The dates that have less than 100 pair of stations remaining after the previous filters, are removed	$\tilde{N}_p > 100$
11.	For each date, the error at each position is calculated as the average difference between the travel times obtained with the differential phase and with a 1D model (Equation 12)	–
12.	The location of the source for each date is the point with the lowest error	–
13.	If the lowest error is in the lower or lateral borders of the grid, the location is removed	–

5. Results

5.1. Tremor Episodes at the Klyuchevskoy Volcanic Group

To detect the occurrence of tremors, the simplified coherence is calculated between all the possible station pairs in Figure 1, between May 2015 and September 2016, using windows of 40 s and averaging windows of 15 min (45 small windows with 50% of overlapping). The stability of the differential phase over the seismic network is estimated by averaging all the simplified coherence magnitudes:

$$\lvert\hat{\gamma}(f,t_0)\rvert = \frac{1}{N_p}\sum_{i=0}^{N-1}\sum_{j=i+1}^{N}\lvert\hat{\gamma}_{i-j}(f,t_0)\rvert \tag{13}$$

where $N = 39$ is the total number of stations, and $N_p = N(N-1)/2 = 780$ is the number of possible pairs between them.

The average of the simplified coherence magnitudes in Figure 6a, shows periods with relatively high stable phase at the end of 2015 and between April and May 2016, which are consistent with previous results obtained through the covariance matrix (Journeau et al., 2022) and machine learning (Steinmann et al., 2024) methods indicating tremor activity in the same periods. The overall average values in this case, in comparison to the station pair IR18-SV13 in Figure 4, are lower as they include station pairs with much lower coherence values. Similar to the results of the covariance matrix analysis, the high coherent spots at low frequencies correspond to strong microseismic noise and teleseismic earthquakes. These events produce signals lasting several minutes which are registered as several 45 s windows with similar differential phases, resulting in high phase coherence values. The changes of the noise $\hat{\gamma}$ values at the beginning and at the end of the analyzed period in Figure 6a are produced by a lower number of stations available, which reduces the expected magnitude of the random cross-spectra sum (Wolfgang & Baschnagel, 2013, p. 69). Contrarily, the noise phase coherence is not affected by changes in the number of stations available, as can be seen in Figure S1 of the Supporting Information S1.

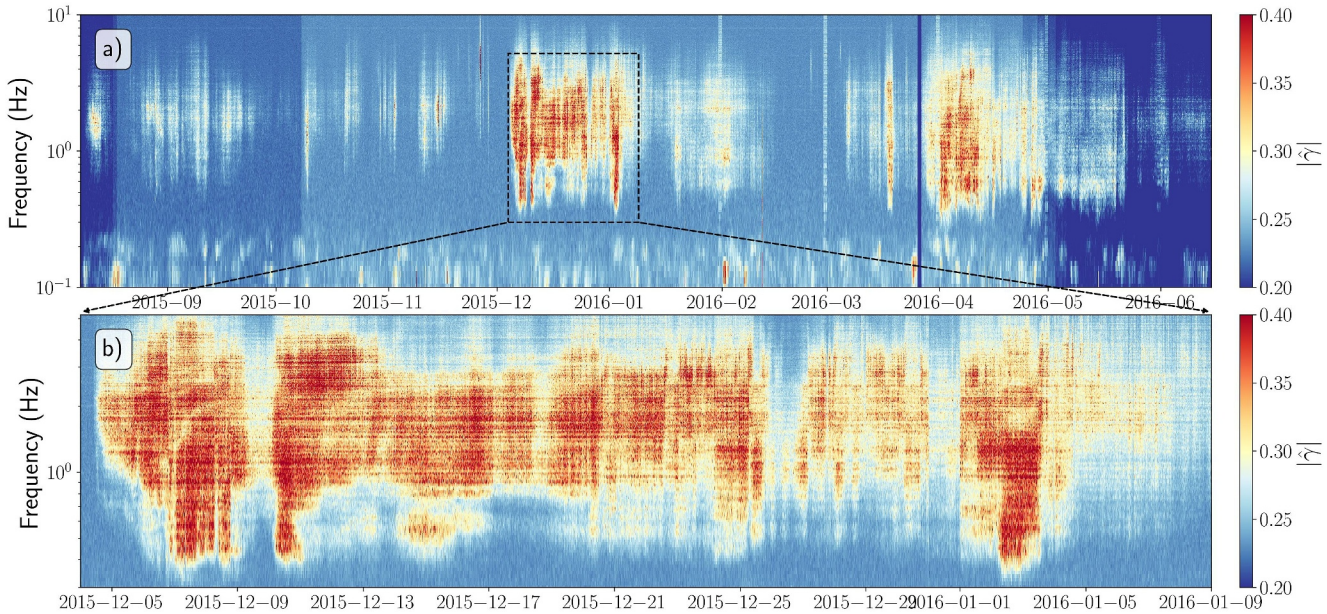

Figure 6. (a) Average of the simplified phase coherence magnitudes between all the possible station pairs between May 2015 and September 2016 (Equation 13). (b) Zoom of the average of the simplified coherence magnitudes between 2015-15-04 and 2016-01-09.

A more detailed observation of the tremor episode at the end of 2015 (Figure 6b) reveals the presence of frequencies that exhibit stability of the phase for long periods. These spectral lines of coherent signal, have also been observed through the covariance matrix method (e.g., Barajas et al., 2023; Caudron, Soubestre, et al., 2022; Journeau et al., 2022; Soubestre et al., 2018).

The approach based on individual station pairs has some advantages over methods that use the whole seismic network. For example, this approach makes possible to study how the coherent wavefield depends on the position of the receivers. Figure 7 shows the amplitude of the phase coherence during a single day for the station pairs joined by the blue and red lines in Figure 1. It is clear that for pair stations closer to the volcanoes (red ring in Figure 1) the coherence magnitude is higher than for those stations further away (blue ring in Figure 1). Figure 7 also shows that the spectral lines at which the differential phase is stable rarely appear at the same frequencies for different station pairs. These observations imply that the observed spectral structure not only depends on the source properties and position, but is also strongly affected by the wave propagation between the source and the receiver. Therefore, the discontinuities observed in Figure 5b are probably produced by this propagation effect, which is highly dependent on the wave travel path and in the position of the stations. This supports a hypothesis of Barajas et al. (2023) suggesting that the interference between multiply scattered waves causes the multiple spectral lines observed during tremors.

5.2. Differential Travel Times During the December 2015–January 2016 Tremor Episode

The differential travel times are calculated for all the possible station pairs, between 0.35 and 5 Hz, during the tremor episode occurring between 2015-12-04 and 2016-01-09 (shown in Figure 6b). The robustness of the measurements for each pair of stations is evaluated with the total number of points contained in all frequency intervals used. In the cases where $\sum_s n_s < 50$, the pair of stations is discarded.

A set of differential times measured at 06:15:00 on 7 December 2015, is illustrated in Figure 8. For each pair of stations, the differential travel time is plotted as an arrow pointing to the station closer to the source. The transparency of each arrow is proportional to the differential travel time between the stations. In some cases, the absence of an arrow between stations occurs because the signal is weak and the filtering process over the differential phase removes all the points or discards the station pair. The general behavior of the travel times suggests the presence of a source close to the station LGN, which is the closest seismic station to the Klyuchevskoy volcano. There is also a second area with high values of differential travel time close to the Tolbachik volcano, probably produced by a secondary source, although in this case, the interpretation is less clear. Movie S1 shows

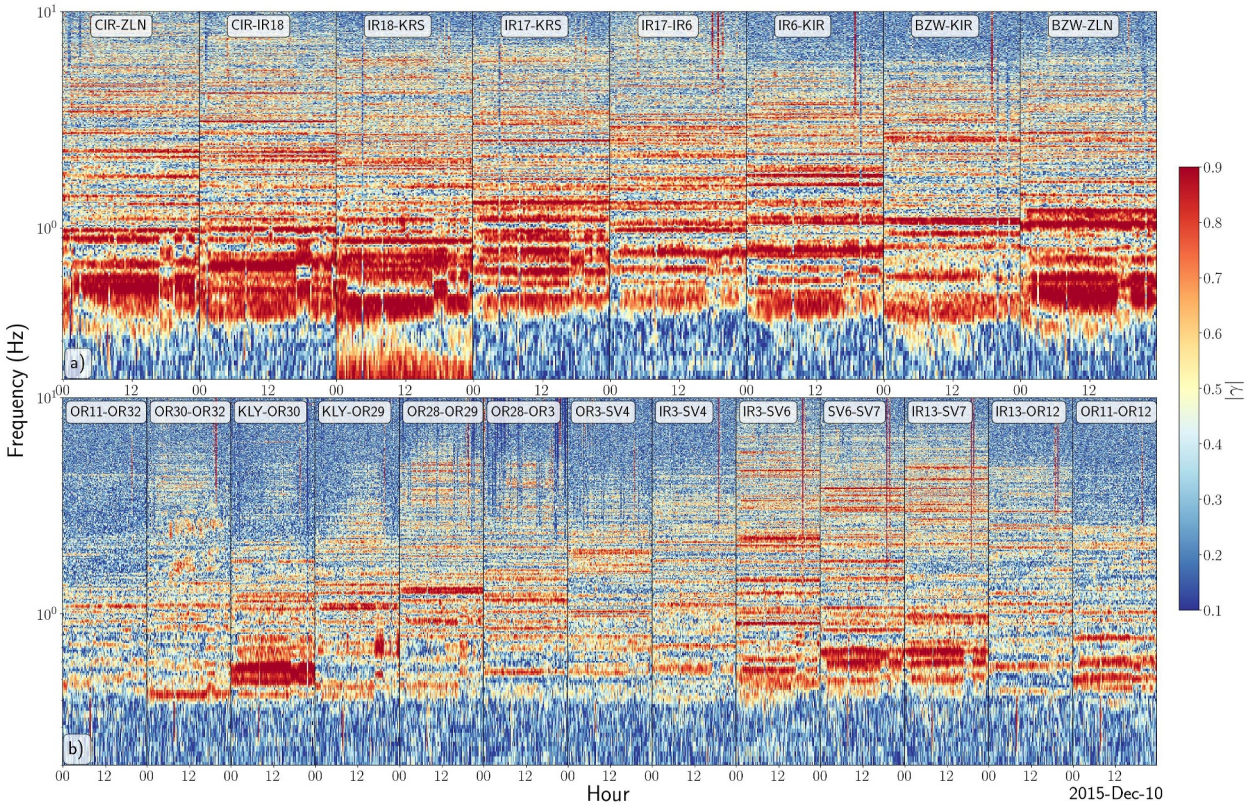

Figure 7. Coherence calculated the same day (2015-12-10) for different station pairs. (a) Coherences for the station pairs joined by the red line in Figure 1. (b) Coherences for the station pairs joined by the blue line in Figure 1.

that the high activity pointing toward the Klyuchevskoy volcano is observed during the whole tremor episode, despite considerable fluctuations in the differential travel times.

5.3. Tremor Source Locations During the December 2015–January 2016 Tremor Episode

We use the differential travel times presented in Section 5.2 to locate sources of tremors corresponding to respective time windows using the procedure described in Section 4.4. The results are illustrated and summarized in Figure 9 with frame (a) showing a comparison between observed and predicted differential travel times for a selected subset of station pairs and the same time window illustrated in Figure 8. Figure 9b shows the source locations obtained for each 15 min window from 2015-12-04 to 2016-01-09, and in color is shown the harmonic mean between the errors in the analyzed period, calculated as

$$\overline{E_r}(\mathbf{r}) = \frac{n_t}{\sum^{n_t}(1/E_r(\mathbf{r}))} \tag{14}$$

where n_t is the number of windows in this period. The harmonic mean is used because the most probable position of the sources is the reciprocal of the error. Figure 9c shows the errors of each window (Equation 12) during the same period. Most locations are concentrated in a 5 km-radius region beneath the Klyuchevskoy and Ushkovsky volcanoes.

The location at depth at different dates, illustrated in Figure 9d, shows that the activity can be separated into two categories: the first one, produced by a single or closely grouped sources extending approximately from 7 to 9 km depth, and the second one extended over a large range of depths up to 50 km depth. This observation is similar to the one by Journeau et al. (2022) who also detected some sources close to the surface and others extended in depth over the whole crust. The migration patterns seen in the latter have been interpreted as possibly associated with fast pressure transients within the plumbing system.

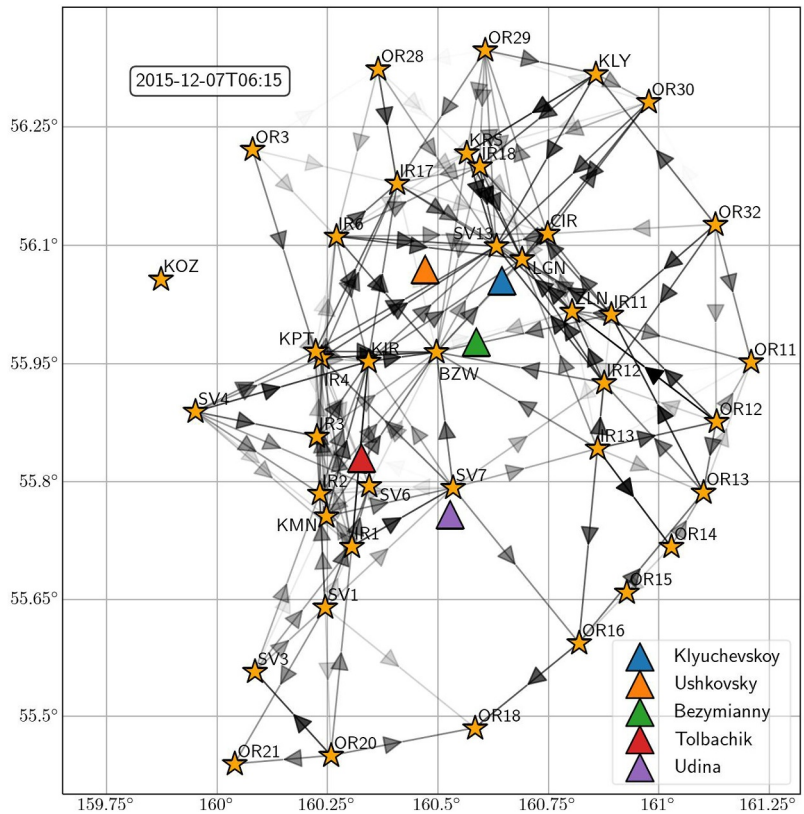

Figure 8. Differential travel times for the 2015-12-07h06:15. The direction of each arrow points to the station closer to the source, and its transparency is proportional to Δt_{i-j}. For visualization purposes, only the station pairs under 30 km of distance from each other are plotted.

At the same time, the source locations obtained in this study and by Journeau et al. (2022) are not identical. This could be a consequence of the domain in which the locations are found: Journeau et al. (2022) obtain the locations in the temporal domain, contrary to this study, where they are estimated in the frequency domain. The results in both methods also depend on the election of several parameters. So far, Journeau et al. (2022) demonstrated that the length of the analyzed time windows $\widetilde{\delta t}$ defined in step 1 of Table 1 is critical to discriminate between shallow and deep sources. Based on their method with relatively small values of, $\widetilde{\delta t}$ they detected many deep tremors characterized by irregular patterns and often appear as bursts of many impulsive events. However, only shallow continuous tremors remained detected after increasing this window length above 55 s.

How the differential phase method "selects" between shallow and deep sources can be done with other parameters. For example, changing the conditions over the coherence magnitude in step 5 of the processing (Table 1), from $|\gamma| > 0.35$ to $0.3 < |\gamma| < 0.9$, changes the "illumination" of the activity depth, as can be seen in Figure 9e, revealing deeper activity in some cases, or showing the presence of the shallow source during periods where it was not observed before. This can be explained by alternative interpretations of the effect of changing the range for $|\gamma|$: first, decreasing the threshold for $|\gamma|$ can be seen as accepting signals with lower phase stability, as the ones produced by small earthquakes occurring at random locations. This has the effect of favoring deeper, less localized activity, as can be seen by comparing Figures 9d and 9e between 2015-12-20 and 2015-12-25. Second, lowering the threshold for $|\gamma|$ can also help to capture activity produced by a stable source during periods when the energy emission is weaker. This is the case of the period between 2016-01-05 and 2016-01-09, in which the phase stability was relatively lower than during the rest of the tremor episode (Figure 6); lowering the threshold for $|\gamma|$ helps to highlight the activity of the shallow stable source (Figure 9e), that was otherwise not captured by stronger conditions on the phase stability (Figure 9d). It is important to note that although the gamma thresholds in Figures 9d and 9e have a big overlap, the effect of filtering in or out some points on the frequency domain has a

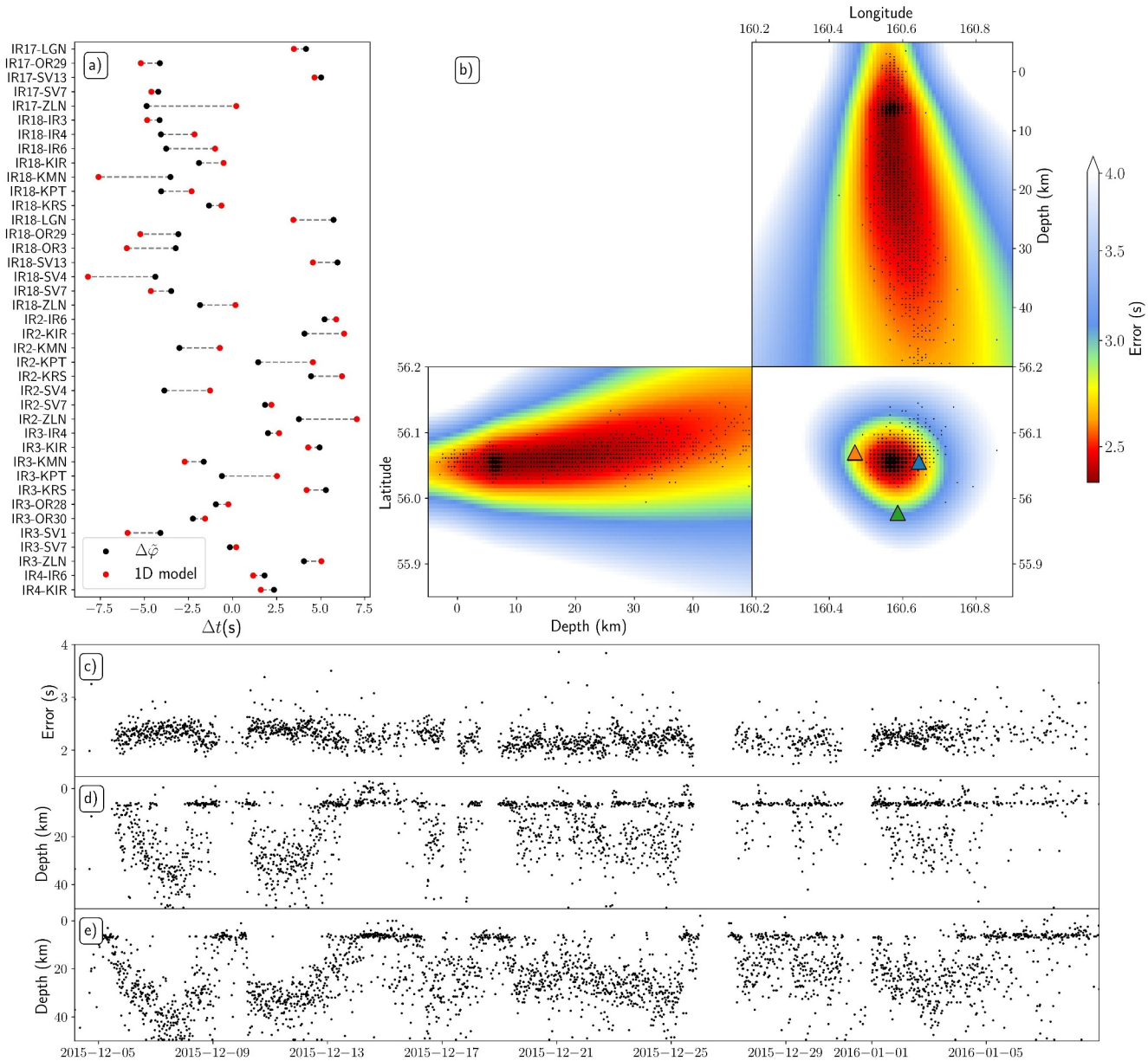

Figure 9. Location of the sources of the tremor episode occurring between 2015-12-04 and 2016-01-09 obtained with the differential phase. (a) Comparison of the differential travel times for the 2015-12-07h06:15, for a subset of station pairs that includes the example station pair IR18-SV13 shown in Figure 5. The differential travel times obtained with the differential phase method (black), and with the 1D model with the source located at the most probable position for this date (red), are joined by the dashed lines. (b) Locations of the sources. The black dots represent the grid points where the source was found, with their size proportional to the number of 15 min windows on each grid point, projected over the respective plane. The color shows the harmonic mean between the errors. (c) Error of each window. (d) Source depth as a function of time for the case with $|\gamma| > 0.35$. (e) Source location as a function of time for the case with $0.3 < |\gamma| < 0.9$.

profound effect on the division, the length and the filtering of the contiguous sets in step 5 (Figure 5b). Overall, these results suggest that the two types of seismic activity (originating by closed localized sources close to the surface and by widespread low-frequency earthquakes), are happening simultaneously within the volcanic system. The conditions over $|\gamma|$ help to "illuminate" one or the other, depending on the overall strength of the wavefield. In that sense, a better way to separate the two types of activity would involve changing the $|\gamma|$ threshold depending on the intensity of the seismic activity, although this is a matter of future research.

6. Discussion

The phase of a signal obtained through the Fourier Transform depends mainly on the beginning of the cycle measured from the arbitrary point designed as time zero (Gatti, 2014, p. 47; O'Shea, 2017) (which is usually the center or the beginning of the time window). For seismic tremors whose source function can be imagined as random, the value of the phase of the signal at individual stations will also be random and usually devoid of physical meaning. For this reason, the studies analyzing the frequency content of tremor signals are often focused on the amplitude of the spectra.

The situation is very different when analyzing the inter-station cross-correlations. When a source produces a signal, the lag time of the most energetic part of a cross-correlation is equal to the difference of the travel times from the source to each of the stations (the differential time) (e.g., Poupinet et al., 1984; Schaff et al., 2004). This lag time, at each frequency, is directly related to the differential phase in the frequency domain (Equation 9). This implies that if signals are emitted continuously from the same position, the phase of the inter-station cross-correlation stabilizes. This stabilization is not observed for the noise whose sources are not localized. Therefore, the fact that the occurrence of tremors correlates with high levels of phase stability, indicates that their sources remain in relatively stable positions during the duration of the analyzed windows.

Such detector based on individual station pairs has some advantages over those using the whole network (e.g., Seydoux et al., 2016) because they can be calculated with only two stations and also can be used to study how the coherent wavefield depends on the position of the receivers. So far, applying the differential phase method to different station pairs in the KVG region has shown that the spectral lines at which the differential phase is stable strongly depend on the station position and are, therefore, strongly affected by the wave propagation between the source and the receiver. This supports a hypothesis of Barajas et al. (2023) suggesting that the interference between multiple scattered waves causes the coherent spectral lines observed during tremors.

Overall, the application of the differential phase method to the KISS data set (39 stations operated in the KVG region in 2015–2016) resulted in a similar pattern of tremor activity as reported by Journeau et al. (2022), including trans-crustal activity extending from the surface to the crust-mantle boundary. However, the location of tremor sources obtained through the differential phase analysis shows that the wavefield is mainly dominated by a cluster of sources located 7–9 km depth. This is consistent with the observed stability of the phase, which is a natural consequence of the stability of the tremor source position.

Particular attention should be paid to the non-uniqueness of the presented analysis, whose results depend on choosing multiple parameters described in Table 1. This non-uniqueness especially affects the results of the source location when applied to complex tremor sequences with multiple sources acting nearly simultaneously. This is a characteristic of the KVG tremors, where shallow and deep activities often coincide. In such a situation, it is better to run a series of analyses with different choices of parameters to ensure that other possible sources of tremors are detected and located. Comparing source locations obtained with phase and amplitude-based differential travel times might also be useful. In the present study, we show that small variations on the thresholds imposed over γ, help to highlight different types of sources over the same window.

Overall, analyzing the differential phase of individual station pairs is complementary to methods based on whole networks and amplitudes of inter-station cross-correlations. In particular, this approach might help to better discriminate between influences of different propagation paths and eventually to identify within the volcanic plumbing systems regions particularly affected by strong scattering thanks to the direct physical relation with the travel time.

Also, thanks to the simple way in which γ is calculated for the seismic network (Equation 13), it is easy to add or remove stations to the analysis, and to compare with results in other networks. The set of observations of differential phases in a seismic network is a natural candidate for machine learning applications that rely on vast amounts of data. Finally, the phase coherence can also be an intermediate tool for assessing the quality of cross-correlation in seismic noise base studies, as some of them estimate travel time variations by analyzing the differential phases in the frequency domain (e.g., Hadziioannou, 2011).

7. Conclusions

We present evidence of the stabilization of the differential phase on inter-station cross-correlations during tremor events in the Klyuchevskoy volcanic system (Figure 2). To quantify the level of stability, we propose two alternative complex-value quantities called phase coherences that take advantage of the cross-spectra to highlight the frequencies where the complex vectors have stable orientations, as a consequence of the phase stability (Figure 3).

We show that the magnitude of the phase coherence for different frequencies is close to one during volcanic tremor episodes. This relation is visible for individual station pairs (Figures 4 and 7), as for the whole seismic array (Figure 6). A comparison of the coherence for different station pairs for the same period, shows that the phase stability does not occur at the same frequencies over the seismic array, suggesting that the path effects are at the origin of these differences (Figure 7).

We estimate the differential travel times for every station pair every 30 min window (Figure 8) by taking advantage of the linearity of the differential phase with the frequency (Equation 9, Figure 5). Travel times estimations obtained by velocity model-based ray tracing, reveal the presence of a stable source, located between 7 and 9 km depth, that remains active during the 1-month tremor episode (Figure 9). The locations also show a second type of tremor sources, located over a wide range of depths. The evidence suggests that both types of source tremors are acting simultaneously. We also show that it is possible to highlight the tremor sources at different depths through variations of the coherence magnitude threshold value in the analysis.

The phase stability observed over many station pairs and frequencies, is a natural consequence of a source emitting energy continuously from the same position within the volcanic system, during extended periods. This is consistent with the long-lasting source found close to the surface with the beamforming during the tremor period (Figures 9d and 9e). The analysis of differential phase together with the phase coherence is a simple and versatile way to study the characteristics of the complex wavefield produced by volcanic tremors.

Appendix A: Comparison With Match Field Processing

There are fundamental differences between the approach and quantities defined in this study and previous studies in Matched Field Processing (MFP). A fundamental aspect of MFP is the existence of a reference wavefield, against which the observations are "matched." In the first step of the method presented here, the estimation of the phase coherence is made without any reference wavefield, but from the inter-two-station cross-correlations. The result of this step is independent of the source location procedure as it quantifies the coherence of the wavefield, and it is obtained without any assumption about the type of waves or their propagation characteristics.

The quantifying statistic of MFP on its different versions is based on the evaluation of the (real-valued) projection of the observed over a reference wavefield (Baggeroer et al., 1993; Gombert & Hawthorne, 2023; Hawthorne & Ampuero, 2018; Schippkus & Hadziioannou, 2022; Wang et al., 2015). The phase coherences, on the other hand, are an average of the complex-valued cross-spectra over several time windows, for the same frequency. Having the projection as the characterizing quantity allows the studies in MFP to have interpretable results with as few as two windows; the phase coherences are not statistically reliable (especially the magnitudes) in this situation. The complex nature of the phase coherences (Equations 6 and 7) is deeply intertwined with the statistical necessity of using a considerable number of windows, as can be visualized from the schematics in Figure 3. Finally, in MFP it is common to sum these projections over several frequencies, either within a small narrowband, across several bands or both (Hawthorne & Ampuero, 2018; Nanni et al., 2021; Wang et al., 2015); this takes advantage of the fact that if the wavefields are coherent, the individual normalized projections should be equal to 1 independently of the frequency, or in the case where the real part of the cross-spectra is used, that two coherent signals have similar phases and the imaginary part of the cross-spectra is approximately zero. However, this is not possible in this study because the phase of the coherence changes with the frequency (this plays a fundamental role in the travel times estimation, as shown in Figure 5), and therefore, summing or averaging them over different frequencies would be conceptually wrong. For example, averaging the phase coherence over several frequencies with completely coherent wavefields will have the opposite effect of reducing its magnitude. This is related to the fact that the phase coherences can only be obtained in the frequency domain, in contrast to MFP, where the quantities can be estimated in both the time and frequency domains.

A quantity also named phase coherence is defined in Hawthorne and Ampuero (2018) to measure the similarity in phase between two observations as

$$C_p = \mathrm{Re}\left[\frac{\mathbf{U}_i(f)\mathbf{U}_j^*(f)}{|\mathbf{U}_i(f)\mathbf{U}_j^*(f)|}\right] \tag{A1}$$

It can be shown that for N windows, C_p and the magnitude of the simplified coherence phase $|\hat{\gamma}_{i-j}|$ are related by:

$$|\hat{\gamma}_{i-j}|^2 = \frac{1}{N} + \frac{2}{N^2}\sum_{n=0}^{N-1}\sum_{m=n+1}^{N} C_{p,n-m} \tag{A2}$$

Data Availability Statement

KISS experiment data are available from the GEOFON datacenter at GFZ-Potsdam (KISS temporary stations: N. Shapiro et al. (2015); permanent stations: https://geofon.gfz-potsdam.de/waveform/archive/network.php?ncode=D0&year=2015).

Acknowledgments
This study was supported by the European Research Council under the European Union Horizon 2020 research and innovation program (Grant Agreement 787399-SEISMAZE). We thank Estelle Delouche for all the discussions and ideas during the formulation of this work. The authors also want to thank Jess Hawthorne, an anonymous reviewer, and the editors, for the careful review of this work and for their valuable input to improve it.

References

Almendros, J., Ibáñez, J., Alguacil, G., Del Pezzo, E., & Ortiz, R. (1997). Array tracking of the volcanic tremor source at Deception Island, Antarctica. *Geophysical Research Letters*, *24*(23), 3069–3072. https://doi.org/10.1029/97gl03096

Baggeroer, A. B., Kuperman, W. A., & Mikhalevsky, P. N. (1993). An overview of matched field methods in ocean acoustics. *IEEE Journal of Oceanic Engineering*, *18*(4), 401–424. https://doi.org/10.1109/48.262292

Ballmer, S., Wolfe, C. J., Okubo, P. G., Haney, M. M., & Thurber, C. H. (2013). Ambient seismic noise interferometry in Hawai'i reveals long-range observability of volcanic tremor. *Geophysical Journal International*, *194*(1), 512–523. https://doi.org/10.1093/gji/ggt112

Barajas, A., Journeau, C., Obara, K., & Shapiro, N. M. (2023). Comparison of continuously recorded seismic wavefields in tectonic and volcanic environments based on the network covariance matrix. *Journal of Geophysical Research: Solid Earth*, *128*(12), e2023JB026784. https://doi.org/10.1029/2023JB026784

Brenguier, F., Campillo, M., Hadziioannou, C., Shapiro, N. M., Nadeau, R. M., & Larose, E. (2008). Postseismic relaxation along the San Andreas fault at Parkfield from continuous seismological observations. *Science*, *321*(5895), 1478–1481. https://doi.org/10.1126/science.1160943

Brenguier, F., Shapiro, N. M., Campillo, M., Ferrazzini, V., Duputel, Z., Coutant, O., & Nercessian, A. (2008). Towards forecasting volcanic eruptions using seismic noise. *Nature Geoscience*, *1*(2), 126–130. https://doi.org/10.1038/ngeo104

Caudron, C., Aoki, Y., Lecocq, T., De Plaen, R., Soubestre, J., Mordret, A., et al. (2022). Hidden pressurized fluids prior to the 2014 phreatic eruption at Mt Ontake. *Nature Communications*, *13*(1), 6145. https://doi.org/10.1038/s41467-022-32252-w

Caudron, C., Soubestre, J., Lecocq, T., White, R. S., Brandsdóttir, B., & Krischer, L. (2022). Insights into the dynamics of the 2010 Eyjafjallajökull eruption using seismic interferometry and network covariance matrix analyses. *Earth and Planetary Science Letters*, *585*, 117502. https://doi.org/10.1016/j.epsl.2022.117502

Chouet, B. A. (1996). Long-period volcano seismicity: Its source and use in eruption forecasting. *Nature*, *380*(6572), 309–316. https://doi.org/10.1038/380309a0

Clarke, D., Zaccarelli, L., Shapiro, N. M., & Brenguier, F. (2011). Assessment of resolution and accuracy of the Moving Window Cross Spectral technique for monitoring crustal temporal variations using ambient seismic noise. *Geophysical Journal International*, *186*(2), 867–882. https://doi.org/10.1111/j.1365-246X.2011.05074.x

Coppola, D., Laiolo, M., Massimetti, F., Hainzl, S., Shevchenko, A. V., Mania, R., et al. (2021). Thermal remote sensing reveals communication between volcanoes of the Klyuchevskoy volcanic group. *Scientific Reports*, *11*(1), 13090. https://doi.org/10.1038/s41598-021-92542-z

Crotwell, H. P., Owens, T. J., & Ritsema, J. (1999). The TauP toolkit: Flexible seismic travel-time and ray-path utilities. *Seismological Research Letters*, *70*(2), 154–160. https://doi.org/10.1785/gssrl.70.2.154

Deichmann, N., & Garcia-Fernandez, M. (1992). Rupture geometry from high-precision relative hypocentre locations of microearthquake clusters. *Geophysical Journal International*, *110*(3), 501–517. https://doi.org/10.1111/j.1365-246x.1992.tb02088.x

Dobretsov, N., Koulakov, I., & Litasov, Y. (2012). Migration paths of magma and fluids and lava compositions in Kamchatka. *Russian Geology and Geophysics*, *53*(12), 1253–1275. https://doi.org/10.1016/j.rgg.2012.10.001

Dodge, D. A., Beroza, G. C., & Ellsworth, W. (1995). Foreshock sequence of the 1992 landers, California, earthquake and its implications for earthquake nucleation. *Journal of Geophysical Research*, *100*(B6), 9865–9880. https://doi.org/10.1029/95jb00871

Dorendorf, F., Wiechert, U., & Wörner, G. (2000). Hydrated sub-arc mantle: A source for the Kluchevskoy volcano, Kamchatka/Russia. *Earth and Planetary Science Letters*, *175*(1), 69–86. https://doi.org/10.1016/S0012-821X(99)00288-5

Droznin, D., Shapiro, N., Droznina, S. Y., Senyukov, S., Chebrov, V., & Gordeev, E. (2015). Detecting and locating volcanic tremors on the Klyuchevskoy group of volcanoes (Kamchatka) based on correlations of continuous seismic records. *Geophysical Journal International*, *203*(2), 1001–1010. https://doi.org/10.1093/gji/ggv342

Endo, E. T., & Murray, T. (1991). Real-time seismic amplitude measurement (RSAM): A volcano monitoring and prediction tool. *Bulletin of Volcanology*, *53*(7), 533–545. https://doi.org/10.1007/bf00298154

Fedotov, S., & Zharinov, N. (2007). On the eruptions, deformation, and seismicity of Klyuchevskoy volcano, Kamchatka in 1986–2005 and the mechanisms of its activity. *Journal of Volcanology and Seismology*, *1*(2), 71–97. https://doi.org/10.1134/s0742046307020017

Fedotov, S. A., Zharinov, N. A., & Gontovaya, L. I. (2010). The magmatic system of the Klyuchevskaya group of volcanoes inferred from data on its eruptions, earthquakes, deformation, and deep structure. *Journal of Volcanology and Geothermal Research*, *4*(1), 1–33. https://doi.org/10.1134/S074204631001001X

Fehler, M. (1983). Observations of volcanic tremor at Mount St. Helens volcano. *Journal of Geophysical Research*, *88*(B4), 3476–3484. https://doi.org/10.1029/JB088iB04p03476

Frank, W. B., Shapiro, N. M., & Gusev, A. A. (2018). Progressive reactivation of the volcanic plumbing system beneath Tolbachik volcano (Kamchatka, Russia) revealed by long-period seismicity. *Earth and Planetary Science Letters*, *493*, 47–56. https://doi.org/10.1016/j.epsl.2018.04.018

Frechet, J. (1985). *Sismogenese et doublets sismiques (Unpublished doctoral dissertation)*. Universite Scientifique et Medicale de Grenoble.

Galina, N. A., & Shapiro, N. M. (2024). Source mechanisms of deep long period earthquakes beneath the Klyuchevskoy volcanic group (Kamchatka, Russia) inferred from S-to-P amplitude ratios. *Journal of Volcanology and Geothermal Research*, *448*, 108049. https://doi.org/10.1016/j.jvolgeores.2024.108049

Galina, N. A., Shapiro, N. M., Droznin, D. V., Droznina, S. Y., Senyukov, S. L., & Chebrov, D. V. (2020). Recurrence of deep long-period earthquakes beneath the Klyuchevskoi volcano group, Kamchatka. *Izvestiya—Physics of the Solid Earth*, *56*(6), 749–761. https://doi.org/10.1134/S1069351320060026

Gatti, P. L. (2014). *Applied structural and mechanical vibrations: Theory and methods*. CRC Press.

Gombert, B., & Hawthorne, J. C. (2023). Rapid tremor migration during few minute-long slow earthquakes in Cascadia. *Journal of Geophysical Research: Solid Earth*, *128*(2), e2022JB025034. https://doi.org/10.1029/2022jb025034

Got, J.-L., Fréchet, J., & Klein, F. W. (1994). Deep fault plane geometry inferred from multiplet relative relocation beneath the south flank of Kilauea. *Journal of Geophysical Research*, *99*(B8), 15375–15386. https://doi.org/10.1029/94jb00577

Green, R. G., Sens-Schönfelder, C., Shapiro, N., Koulakov, I., Tilmann, F., Dreiling, J., et al. (2020). Magmatic and sedimentary structure beneath the Klyuchevskoy volcanic group, Kamchatka, from ambient noise tomography. *Journal of Geophysical Research: Solid Earth*, *125*(3), e2019JB018900. https://doi.org/10.1029/2019JB018900

Hadziioannou, C. (2011). *Ondes sismiques en milieu complexe: mesure des variations temporelles des vitesses. Theses*. Université de Grenoble. Retrieved from https://theses.hal.science/tel-00564110

Hawthorne, J., & Ampuero, J. (2018). A phase coherence approach to identifying co-located earthquakes and tremor. *Geophysical Journal International*, *209*(2), 623–642.

Heaton, T. H. (1975). Tidal triggering of earthquakes. *Geophysical Journal International*, *43*(2), 307–326. https://doi.org/10.1111/j.1365-246x.1975.tb00637.x

Hotz, T. (2013). Extrinsic vs intrinsic means on the circle. In *International conference on geometric science of information* (pp. 433–440).

Hughes, B. D. (1996). *Random walks and random environments*. Oxford University Press.

Ito, A. (1985). High resolution relative hypocenters of similar earthquakes by cross-spectral analysis method. *Journal of Physics of the Earth*, *33*(4), 279–294. https://doi.org/10.4294/jpe1952.33.279

Ivanov, A., Koulakov, I. Y., West, M., Jakovlev, A., Gordeev, E., Senyukov, S., & Chebrov, V. (2016). Magma source beneath the Bezymianny volcano and its interconnection with Klyuchevskoy inferred from local earthquake seismic tomography. *Journal of Volcanology and Geothermal Research*, *323*, 62–71. https://doi.org/10.1016/j.jvolgeores.2016.04.010

Journeau, C., Shapiro, N. M., Peltier, A., Ferrazzini, V., Soubestre, J., Duputel, Z., et al. (2023). Tracking changes in the co-eruptive seismic tremor associated with magma degassing at Piton de La Fournaise volcano. *Journal of Volcanology and Geothermal Research*, *444*, 107936. https://doi.org/10.1016/j.jvolgeores.2023.107936

Journeau, C., Shapiro, N. M., Seydoux, L., Soubestre, J., Ferrazzini, V., & Peltier, A. (2020). Detection, classification, and location of seismovolcanic signals with multicomponent seismic data: Example from the Piton de La Fournaise volcano (La Réunion, France). *Journal of Geophysical Research: Solid Earth*, *125*(8), e2019JB019333. https://doi.org/10.1029/2019jb019333

Journeau, C., Shapiro, N. M., Seydoux, L., Soubestre, J., Koulakov, I. Y., Jakovlev, A. V., et al. (2022). Seismic tremor reveals active trans-crustal magmatic system beneath Kamchatka volcanoes. *Science Advances*, *8*(5), eabj1571. https://doi.org/10.1126/sciadv.abj1571

Konstantinou, K. I., & Schlindwein, V. (2002). Nature, wavefield properties and source mechanism of volcanic tremor: A review. *Journal of Volcanology and Geothermal Research*, *119*(1–4), 161–187. https://doi.org/10.1016/S0377-0273(02)00311-6

Koulakov, I., Abkadyrov, I., Al Arifi, N., Deev, E., Droznina, S., Gordeev, E. I., et al. (2017). Three different types of plumbing system beneath the neighboring active volcanoes of Tolbachik, Bezymianny, and Klyuchevskoy in Kamchatka. *Journal of Geophysical Research: Solid Earth*, *122*(5), 3852–3874. https://doi.org/10.1002/2017JB014082

Koulakov, I., Shapiro, N. M., Sens-Schönfelder, C., Luehr, B. G., Gordeev, E. I., Jakovlev, A., et al. (2020). Mantle and crustal sources of magmatic activity of Klyuchevskoy and surrounding volcanoes in Kamchatka inferred from earthquake tomography. *Journal of Geophysical Research: Solid Earth*, *125*(10), e2020JB020097. https://doi.org/10.1029/2020jb020097

Kuperman, W., & Turek, G. (1997). Matched field acoustics. *Mechanical Systems and Signal Processing*, *11*(1), 141–148. https://doi.org/10.1006/mssp.1996.0066

Levin, V., Droznina, S. Y., Gavrilenko, M., Carr, M. J., & Senyukov, S. L. (2014). Seismically active subcrustal magma source of the Klyuchevskoy volcano in Kamchatka, Russia. *Geology*, *42*(11), 983–986. https://doi.org/10.1130/G35972.1

Levin, V., Shapiro, N., Park, J., & Ritzwoller, M. (2002). Seismic evidence for catastrophic slab loss beneath Kamchatka. *Nature*, *418*(6899), 763–767. https://doi.org/10.1038/nature00973

Margrave, G. F., & Lamoureux, M. P. (2019). *Numerical methods of exploration seismology: With algorithms in MATLAB®*. Cambridge University Press.

McGillem, C. D., & Cooper, G. R. (1991). Continuous and discrete signal and system analysis. (No Title).

McNutt, S. R., & Nishimura, T. (2008). Volcanic tremor during eruptions: Temporal characteristics, scaling and constraints on conduit size and processes. *Journal of Volcanology and Geothermal Research*, *178*(1), 10–18. https://doi.org/10.1016/j.jvolgeores.2008.03.010

Michele, M., Chiaraluce, L., Di Stefano, R., & Waldhauser, F. (2020). Fine-scale structure of the 2016–2017 central Italy seismic sequence from data recorded at the Italian national network. *Journal of Geophysical Research: Solid Earth*, *125*(4), e2019JB018440. https://doi.org/10.1029/2019jb018440

Nanni, U., Gimbert, F., Roux, P., & Lecointre, A. (2021). Observing the subglacial hydrology network and its dynamics with a dense seismic array. *Proceedings of the National Academy of Sciences of the United States of America*, *118*(28), e2023757118. https://doi.org/10.1073/pnas.2023757118

O'Shea, P. (2017). Phase measurement. In *Measurement, instrumentation, and sensors handbook* (pp. 24–31). CRC Press.

Portnyagin, M., Hoernle, K., Avdeiko, G., Hauff, F., Werner, R., Bindeman, I., et al. (2005). Transition from arc to oceanic magmatism at the Kamchatka-Aleutian junction. *Geology*, *33*(1), 25–28. https://doi.org/10.1130/G20853.1

Poupinet, G., Ellsworth, W., & Frechet, J. (1984). Monitoring velocity variations in the crust using earthquake doublets: An application to the Calaveras fault, California. *Journal of Geophysical Research*, *89*(B7), 5719–5731. https://doi.org/10.1029/jb089ib07p05719

Prieto, G. A. (2022). The multitaper spectrum analysis package in Python. *Seismological Research Letters*, *93*(3), 1922–1929. https://doi.org/10.1785/0220210332

Roman, D. C., & Cashman, K. V. (2006). The origin of volcano-tectonic earthquake swarms. *Geology*, *34*(6), 457. https://doi.org/10.1130/G22269.1

Rydelek, P. A., & Hass, L. (1994). On estimating the amount of blasts in seismic catalogs with Schuster's method. *Bulletin of the Seismological Society of America*, *84*(4), 1256–1259. https://doi.org/10.1785/bssa0840041256

Schaff, D. P., Bokelmann, G. H., Ellsworth, W. L., Zanzerkia, E., Waldhauser, F., & Beroza, G. C. (2004). Optimizing correlation techniques for improved earthquake location. *Bulletin of the Seismological Society of America*, *94*(2), 705–721. https://doi.org/10.1785/0120020238

Schippkus, S., & Hadziioannou, C. (2022). Matched field processing accounting for complex earth structure: Method and review. *Geophysical Journal International*, *231*(2), 1268–1282. https://doi.org/10.1093/gji/ggac240

Schuster, A. (1897). On lunar and solar periodicities of earthquakes. *Proceedings of the Royal Society of London*, *61*(369–377), 455–465.

Senyukov, S., Droznina, S. Y., Nuzhdina, I., Garbuzova, V., & Kozhevnikova, T. Y. (2009). Studies in the activity of Klyuchevskoi volcano by remote sensing techniques between January 1, 2001 and July 31, 2005. *Journal of Volcanology and Seismology*, *3*(3), 191–199. https://doi.org/10.1134/s0742046309030051

Seydoux, L., Shapiro, N. M., de Rosny, J., Brenguier, F., & Landès, M. (2016). Detecting seismic activity with a covariance matrix analysis of data recorded on seismic arrays [Software]. *Geophysical Journal International*, *204*(3), 1430–1442. https://doi.org/10.1093/gji/ggv531

Shapiro, N., Sens-Schönfelder, C., Lühr, B., Weber, M., Abkadyrov, I., Gordeev, E., et al. (2015). Klyuchevskoy volcanic group experiment (KISS) [Dataset]. https://doi.org/10.14470/K47560642124

Shapiro, N. M., Droznin, D., Droznina, S. Y., Senyukov, S., Gusev, A., & Gordeev, E. (2017). Deep and shallow long-period volcanic seismicity linked by fluid-pressure transfer. *Nature Geoscience*, *10*(6), 442–445. https://doi.org/10.1038/ngeo2952

Shapiro, N. M., Sens-Schönfelder, C., Lühr, B. G., Weber, M., Abkadyrov, I., Gordeev, E. I., et al. (2017). Understanding Kamchatka's extraordinary: Volcano cluster. *Eos: Transactions, American Geophysical Union*, *98*(7), 12–17. https://doi.org/10.1029/2017eo071351

Shapiro, N. M., Soubestre, J., & Journeau, C. (2024). Network-based analysis of seismo-volcanic tremors. In Z. Spica, & C. Caudron (Eds.), *Modern volcano monitoring*. Springer Nature.

Shearer, P. M. (1997). Improving local earthquake locations using the L1 norm and waveform cross correlation: Application to the Whittier Narrows, California, aftershock sequence. *Journal of Geophysical Research*, *102*(B4), 8269–8283. https://doi.org/10.1029/96jb03228

Soubestre, J., Chouet, B., & Dawson, P. (2021). Sources of volcanic tremor associated with the summit caldera collapse during the 2018 east rift eruption of Kīlauea volcano, Hawai'i. *Journal of Geophysical Research: Solid Earth*, *126*(6), e2020JB021572. https://doi.org/10.1029/2020JB021572

Soubestre, J., Seydoux, L., Shapiro, N., De Rosny, J., Droznin, D., Droznina, S. Y., et al. (2019). Depth migration of seismovolcanic tremor sources below the Klyuchevskoy volcanic group (Kamchatka) determined from a network-based analysis. *Geophysical Research Letters*, *46*(14), 8018–8030. https://doi.org/10.1029/2019gl083465

Soubestre, J., Shapiro, N. M., Seydoux, L., de Rosny, J., Droznin, D. V., Droznina, S. Y., et al. (2018). Network-based detection and classification of seismovolcanic tremors: Example from the Klyuchevskoy volcanic group in Kamchatka. *Journal of Geophysical Research: Solid Earth*, *123*(1), 564–582. https://doi.org/10.1002/2017jb014726

Steinmann, R., Seydoux, L., Journeau, C., Shapiro, N. M., & Campillo, M. (2024). Comparison of continuously recorded seismic wavefields in tectonic and volcanic environments based on the network covariance matrix. *ESS Open Archive*. https://doi.org/10.22541/essoar.168614505.54607219/v1

Valoroso, L., Chiaraluce, L., Piccinini, D., Di Stefano, R., Schaff, D., & Waldhauser, F. (2013). Radiography of a normal fault system by 64,000 high-precision earthquake locations: The 2009 L'Aquila (central Italy) case study. *Journal of Geophysical Research: Solid Earth*, *118*(3), 1156–1176. https://doi.org/10.1002/jgrb.50130

Waldhauser, F., & Ellsworth, W. L. (2000). A double-difference earthquake location algorithm: Method and application to the northern Hayward fault, California. *Bulletin of the Seismological Society of America*, *90*(6), 1353–1368. https://doi.org/10.1785/0120000006

Wang, J., Templeton, D. C., & Harris, D. B. (2015). Discovering new events beyond the catalogue—Application of empirical matched field processing to Salton Sea geothermal field seismicity. *Geophysical Journal International*, *203*(1), 22–32. https://doi.org/10.1093/gji/ggv260

Wolfgang, P., & Baschnagel, J. (2013). *Stochastic processes: From physics to finance*. Springer.

Yates, A. (2023). *Towards accurate monitoring of explosive volcanoes using seismic noiseinterferometry (Unpublished doctoral dissertation)*. Université Savoie Mont Blanc.

Yogodzinski, G., Lees, J., Churikova, T., Dorendorf, F., Wöerner, G., & Volynets, O. (2001). Geochemical evidence for the melting of subducting oceanic lithosphere at plate edges. *Nature*, *409*(6819), 500–504. https://doi.org/10.1038/35054039